Article

Effect of Cooling Rate on Crystallization Behavior during Solidification of Hyper Duplex Stainless Steel S33207: An In-Situ Confocal Microscopy Study

Yong Wang [1, 2] and Wangzhong Mu [2,*]

[1] Key Laboratory for Ferrous Metallurgy and Resources Utilization of Ministry of Education & Hubei Provincial Key Laboratory for New Processes of Ironmaking and Steelmaking, Wuhan University of Science and Technology, Wuhan 430081, China

[2] Department of Materials Science and Engineering, KTH Royal Institute of Technology, SE-100 44 Stockholm, Sweden

* Correspondence: wmu@kth.se

Abstract: Hyper duplex stainless steels, HDSS, are a new alloy group of duplex stainless steels with the highest corrosion resistance and mechanical properties among the existing modern stainless steel. Due to the addition of extra high content of alloying elements, e.g. Cr, Ni, Mo, etc., the crystallization behavior of the δ-ferrite from liquid is of vital importance for controlling the steel properties. In this work, the effect of cooling rate (i.e. 4°C/min and 150 °C/min) on the growth process of δ-ferrite in S33207 during the solidification process was investigated using high-temperature confocal scanning laser microscopy (HT-CLSM) in combination with electron microscopies and thermodynamic calculation. The results showed that the solidification mode of S33207 steel was a ferrite-austenite type (FA mode). L→δ transformation occurred at a certain degree of supercooling, and merging occurred during the growth of δ phase dendrites. Similar microstructures were observed after solidification under these two different cooling rates. The variation of area fraction of δ ferrite at the free surface and temperature as well as time during solidification of S33207 steels were calculated, which can be expressed as $f_{\delta,\text{slow}} = 1-\exp(-7.4\times10^{-8}\times t^{3.4})$ and $f_{\delta,\text{fast}} = 1-\exp(-1.2\times10^{-3}\times t^{1.9})$ at a cooling rate of 4 °C/min and 150 °C/min, respectively. The current HT-CLSM study provides an in-situ experimental evidence to confirm that a low cooling rate favored the growth of primary δ-ferrite, whereas a high cooling rate favored the nucleation of primary δ-ferrite during the solidification process. The post microstructure as well as composition evolution is also briefly investigated. This work shed light on the real time insights for the crystallization behavior of hyper duplex stainless steels during solidification, which aims to contribute the process control of manufacturing of this steel grade.

Keywords: solidification; cooling rate; hyper duplex stainless steel; high-temperature confocal scanning laser microscope

1. Introduction

Duplex stainless steel (DSS) has shown increasing demands for applications in important industrial areas such as deep-sea pipelines and submarines [1, 2] and petrochemical industries [1, 3] due to their excellent corrosion resistance and mechanical properties [4, 5]. The desired properties of DSS are mainly corrected with the precise control of the fraction of ferrite and austenite. Despite the very successful applications and experience of DSSs, the development of highly alloyed DSSs has been very active since there are still areas where the corrosion resistance of current DSSs is insufficient for a long service life or at higher temperatures. Based on this challenge, UNS S33207 hyper DSS (marked as S33207 from herein) which has the highest corrosion resistance and strength among the existing modern DSSs has been developed [6-9].

 doi:10.20944/preprints202305.0501.v1

DSSs are designed to solidify with ferrite as the parent phase, with subsequent austenite formation occurring in the solid state, implying that the solidification process plays an important role in the dual-phase microstructure control [10, 11]. That is to say, the changes in the fraction of ferrite and austenite of DSSs are due to different solidification conditions. It is recognized that the cooling rate has an important effect on the microstructure evolution of steel. High-temperature confocal laser scanning microscopy (HT-CLSM) has provided a convenient possibility of making an in-situ observation of the solidification and post-microstructure evolution of various alloy grades, including low carbon steels [12-14] superalloys [15, 16] and stainless steels [17-19]. Wu et al.[20] observed the solidification microstructure evolution of 316LN stainless steel at different cooling rates, finding that the shape of ferrite changed from island-like to lacy-like with increasing cooling rates. Li et al. [21] found that the start and final temperatures of solidification decreased and the δ-ferrite volume fraction increased with the increment of cooling rate in 316H austenitic stainless steel. Zhang et al. [22] also reported that the nucleation temperature of the δ-ferrite phase gradually decreased, which affected the δ-ferrite/γ-austenite formation process in 18Cr-Al-Si ferritic heat-resistant stainless steel. Sun et al. [17] studied the characteristics of the δ→γ phase transformations at different cooling rates on the surface of S31308 DSS by HT-CLSM. They found that the γ-cells preferred to precipitate along the δ/δ grain boundaries with a flaky pattern, and their fronts were jagged in shape at the slow cooling rate, but in a needle-like feature at the rapid cooling rate. Later, they further studied the effect of different N contents on the solid-state δ→γ phase transformations, and concluded that higher N content promoted the nucleation and growth of the γ-phase during the δ→γ transformation by increasing both the starting and finishing temperatures of the phase transformation [23]. Shin et al. [24] have studied the effect of cooling rate after heat treatment on pitting corrosion of S32750 DSS and they found that the ferrite volume fraction increased with the increase in the cooling rate. In a former study by the authors, the solidification behavior of different grades of DSSs have been investigated in-situ [25] using a combinational approach of HT-CLSM and Differential scanning calorimetry (DSC) [26]. However, there is no in-situ observation on the solidification process of hyper duplex stainless steel S33207 under different cooling rates.

Studies have demonstrated that the solidification process of DSSs has a great influence on their performance. Changing the cooling rate is one of the important methods to control the fraction of ferrite and austenite phases. S33207 hyper DSS has quite high Cr contents (32%) compared to other super DSSs, which results in high corrosion resistance, yield strength and superior fatigue features. Therefore, understanding its solidification behavior is of great interest for the subsequent annealing homogenization treatment process. The characteristics of the δ formation and growth during the solidification process were observed on the sample surface of DSS S33207 at different cooling rates by the HT-CLSM in this work. The microstructure and element distribution of HT-CLSM solidified samples were characterized. This work is of great significance to the control of the solidification process of DSS S33207.

2. Materials and Methods

DSC was used to measure the solidification temperature of DSSs before the HT-CLSM observation, the results can be found in a previous work [25]. HT-CLSM was utilized to study the microstructure evolution of DSS S33207 during solidification at different cooling rates. A special and as-cast DSS was used in this experiment, whose chemical composition is shown in Table 1. For HT-CLSM experiments, the diameter of the sample is 4 mm and the thickness is 1.5 mm. All the slices were grounded by 800, 1200, 2000 SiC papers and polished by 3 μm and 1 μm diamond pastes. The processed sample was filled with Al_2O_3 crucible ((Φ 5.5 mm O.D., Φ 4.5 mm I.D., 5.0 mm height) and put into the ellipsoidal chamber of the HT-CLSM instrument. The chamber was cleaned thoroughly by a cycle of vacuum (less than 4.5×10−5 torr) and purging with a high purity Ar (purity>99.9999%) passing a 300 ºC Mg column. The temperature was measured by using a Type B (PtRh30%-PtRh6%) thermocouple at the bottom of the holder of the crucible. The steel samples were first heated to 1500 ºC at a rate of 20 ºC /min and kept for 2 min for melt stabilization, and followed by cooling at two different cooling rates of 4 ºC /min and 150 ºC /min, respectively.

Preprints (www.preprints.org) | NOT PEER-REVIEWED | Posted: 8 May 2023 doi:10.20944/preprints202305.0501.v1

Table 1. Chemical compositions of S33207 steel samples (mass percent, %)

Steel	C	Cr	Ni	Cu	Mn	Mo	Ti	Nb	V	S	O	N
S33207	0.015	31.2	7	0.2	0.7	3.46	0.01	0.01	0.07	0.001	0.004	0.47

3. Results and discussion

3.1. In-situ microstructures of steel at different cooling rates

The solidification phase diagram and phase fraction during the solidification of S33207 steel was calculated by Scheil-Gulliver and equilibrium modules in Thermo-Calc, the results are shown in Figure 1. The Scheil-Gulliver module can calculate the actual solidification path of DSS S33207 under a non-equilibrium state, and provide a basis for the solidification sequence in-situ observation by HT-CLSM. According to Figure 1, the solidification sequence of S33207 steel calculated by both modules belonged to the Ferrite-Austenite mode (FA): L(liquid)→L+δ (ferrite)→L+δ+γ (austenite). It indicated that the δ-ferrite phase started to form first and δ→γ transformation at the terminal stage of solidification of steel. The morphologies of crystallization phases can vary depending on the cooling rate, which is discussed in detail in the following part.

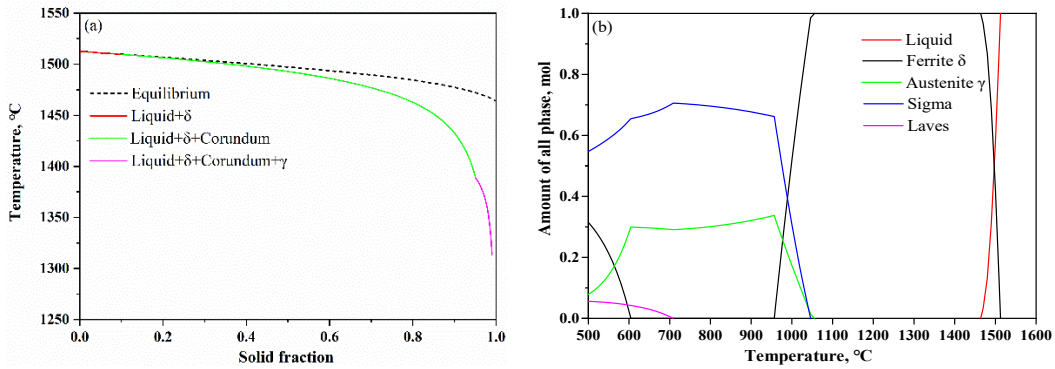

Figure 1. Scheil-Gulliver solidification diagram (a) and equilibrium solidification diagram (b) of S33207 steel

Figure 2 presents some representative micrographs of phase formation during the solidification process of DSS S33207 by in-situ observation at a cooling rate is 4 °C/min. When the molten steel was supercooled to 1482.7 °C, the L→δ transformation began to occur, and the formation of cellular δ phase can be observed on the surface of the sample. It should be pointed out that a thin δ layer formed outside of the liquid poor at the beginning of the solidification (Figure 2 (a)). It is generally believed that the crucible provided a core for heterogeneous nucleation of new phase formation during the solidification observation by HT-CLSM. Due to the slow cooling rate of liquid steel, pro-eutectoid δ-ferrite solidified in the form of cellular crystals. With the decrease in temperature, the number of δ-ferrite nuclei increased and the grains gradually grew up and coarsened. When the δ-ferrite cell grew to some extent, some cells gradually approached and merged into a large irregular δ cell, and there was no obvious boundary between the cells after merging (Figure 2 (b)). With further cooling, more δ cells would merge together and the remaining liquid between the δ cells became less and less (Figure 2 (c)). The growth of δ-ferrite was completed when the area of δ cells was not obviously increased based on the HT-CLSM observations. Some amount of liquid was still present after the ferrite growth was complete (Figure 2 (d)), which has been reported in previous works [27, 28].

Preprints (www.preprints.org) | NOT PEER-REVIEWED | Posted: 8 May 2023 doi:10.20944/preprints202305.0501.v1

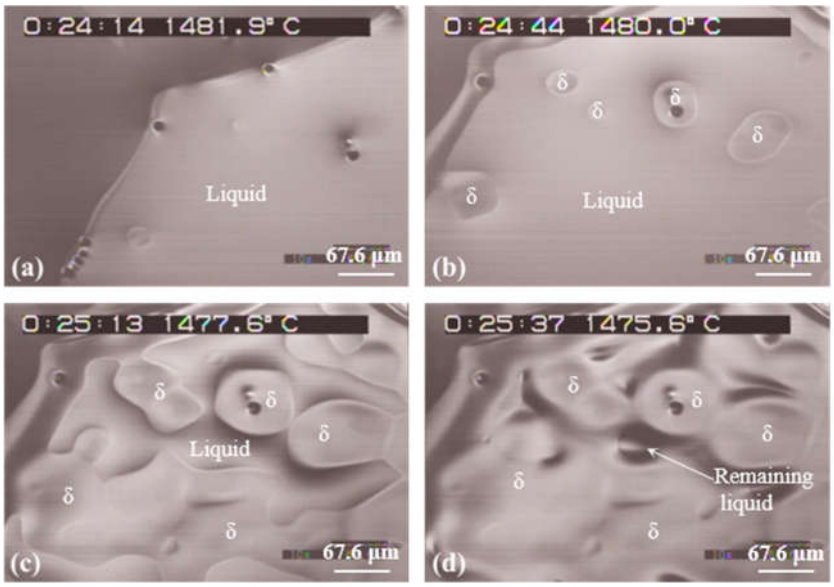

Figure 2. Growth process and characteristics of δ-ferrite phase at a cooling rate of 4 °C/min

The nucleation and growth process of the δ-ferrite phase with a cooling rate is 150 °C/min is shown in Figure 3. It should be mentioned that the focus of the initial stage of δ-ferrite nucleation from the liquid poor was not clear enough during the HT-CLSM observations at this high cooling rate. Therefore, the formation temperature of δ-ferrite on the liquid surface was not determined correctly. More δ-ferrite cells can be formed simultaneously at the beginning of the solidification process compared to that of the low cooling rate. This indicated that a fast cooling rate favored primary δ-ferrite nucleation. The increase of the cooling rate during the solidification process of steel increased the supercooling of the liquid steel composition, which promoted the increase of the nucleation rate of δ-ferrite phase, which was beneficial to the refinement of δ cell crystals. Besides, the δ-ferrite phase formed at a higher temperature than that of a slow cooling rate (Figure 3 (a)). This tendency was opposite to previous works [22, 29], where a higher cooling rate resulted in a higher supercooling degree of melt and lower crystallization temperature of δ-ferrite. The reason for the different results in the current work should be studied further. The δ-ferrite grew quickly and a similar merging phenomenon was observed with a temperature decrease. Besides, clear interphase boundary that usually separated these phases was observed (Figure 3 (b)). Under a high cooling rate, an obvious δ-ferrite growth layer was observed outside of the original δ cells due to the unstable growth characteristics of δ cells. The liquid area was pushed by the growth of δ-ferrite during the late stage of the solidification process and then a volume shrinkage occurred between δ-ferrite phase boundaries (Figure 3 (c)). The growth rate of δ-ferrite decreased due to less liquid left at this stage. With a further decrease of temperature, the area of δ-ferrite slowly increased and kept at a stable value (Figure 3 (d)). This remaining liquid area was the place where the localized transformation from δ-ferrite to γ-austenite at a lower temperature [22]. Generally, the concentration of segregated elements increased greatly in the remaining liquid, where serious segregation happened [27]. The segregation can result in the decrease of solidifying temperatures for steel. Along with time passing, the δ-ferrite to γ-austenite transformation started at the δ-ferrite boundaries (Figure 3 (e), (f)). This finding is similar to that of Li et al. [21] and Zhang et al. [22], who reported that δ→γ transformation occurred accompanied by significant volume shrinkage.

However, the start temperature of δ-γ transformation cannot be obtained accurately based on current observations. It was reported that the δ-γ phase transformation started earlier and occurred at a higher temperature in S32101 DSS based on the concentric solidification technique with the increase of cooling rate [18]. However, Sun et al. [17] found that starting temperature of the δ-γ transformation at the slow cooling rate was higher than that at the rapid cooling rate in an S31308 DSS. Besides, the slow cooling rate more strongly favored nucleation and growth of γ-phase than the

Preprints (www.preprints.org) | NOT PEER-REVIEWED | Posted: 8 May 2023 doi:10.20944/preprints202305.0501.v1

rapid cooling rate due to the fact that higher diffusion rates of elements and longer diffusion time were obtained at a lower cooling rate.

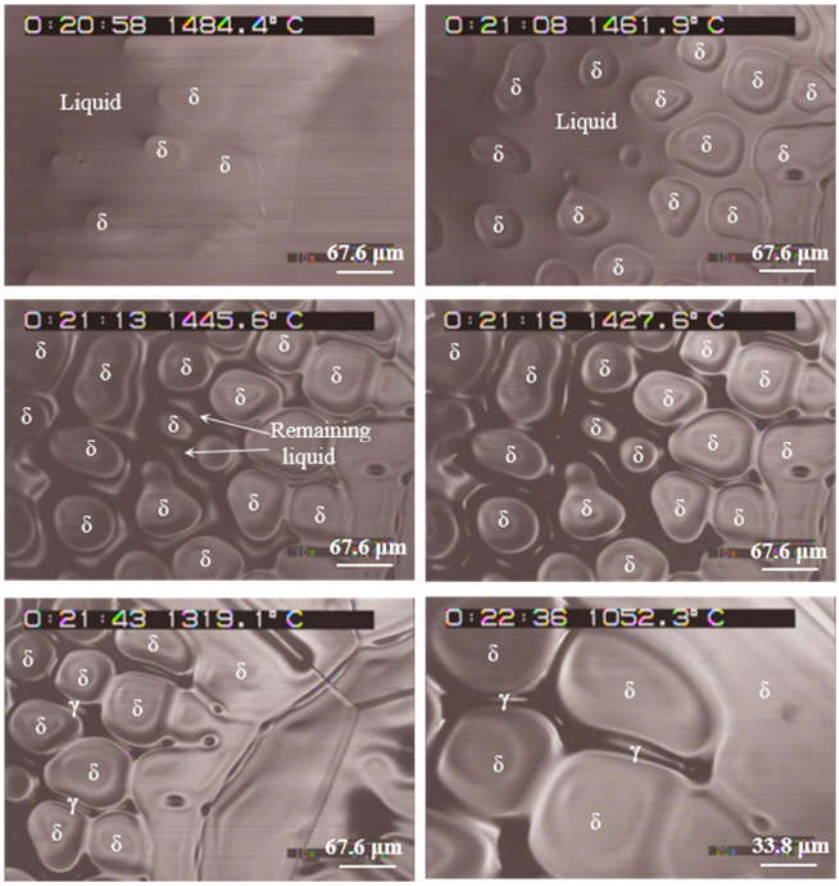

Figure 3. Growth process and characteristics of δ phase at a cooling rate of 150 °C/min

The area fraction of ferrite in multiple sets of video screenshots during the solidification process at different cooling rates and temperatures were measured by ImageJ software, and the Avrami equation was used to fitting the relationship between the area fraction of ferrite and time and temperature, the results are shown in Figure 4. The Avrami equation (1) [30, 31] describes the crystallization of undercooled liquids into a solid state.

$$f_\delta = 1 - \exp(-k \cdot t^n) \quad (1)$$

where f_δ is the area fraction of δ ferrite, n is the Avrami coefficient, k is the overall growth rate constant, and t is the solidification time after the nucleation of δ ferrite.

It can be seen from Figure 4 (a) that the area fraction of δ ferrite increases with time, and it has a higher growth rate at a high cooling rate. In addition, the growth rate of δ ferrite shows smaller values at the initial and late stages of the solidification and higher value at the stable stage of the solidification process. As mentioned before, the formation point of δ ferrite in liquid was not obtained correctly, so the area fraction of δ ferrite curve was obtained using the Avrami fitting function when the fitted linear correlation coefficient (R^2) was greater than 95%. Furthermore, the area fraction of ferrite is less than 1 due to the adverse effects of undulating cellular morphology on the depth of observation field in the HT-CLSM image, which is more prominent at a high cooling rate. The fitted equations between the area fraction of δ ferrite (f_δ) and time in the cases of cooling rate of 4 °C/min and 150 °C/min are expressed by equations (2) and (3), respectively. The rate constant k represents the velocity at which liquid transforms to solid. According to the fitted equations, the larger growth rate constant can be obtained under the fast cooling rate, which indicates the larger growth rate of δ ferrite. This can be explained by the different number density of nucleation and total growth time for

 doi:10.20944/preprints202305.0501.v1

the δ ferrite. Specifically, the time for δ ferrite growth under the slow cooling rate is almost three times longer than that in the fast cooling rate.

$$f_{\delta,\text{fast}} = 1 - \exp(-1.2 \times 10^{-3} \times t^{1.9}) \quad (2)$$

$$f_{\delta,\text{slow}} = 1 - \exp(-7.4 \times 10^{-8} \times t^{3.4}) \quad (3)$$

The growth of δ ferrite finishes in a narrow temperature range (less than 10 °C) at the cooling rate of 4°C/min, while a much wider temperature is obtained at the cooling rate of 150 °C/min (Figure 4 (b)). In particular, δ ferrite starts to form at a higher temperature and the growth ends at a lower temperature in the case of fast cooling compared to that of slow cooling. The on-set and peak temperatures of S33207 steel are 1479.2 ºC and 1481.3 ºC obtained by DSC measurements, where the on-set temperature relates to the δ-ferrite formation. It is known that supercooling phenomenon usually occurs in the solidification process of steel, so the ferrite formation temperature should be lower than the liquidus temperature of steel. From the in-situ CLSM observation results of the solidification process, the δ-ferrite formation temperature was higher than the liquidus temperature of steel under two different cooling rates. This can be attributed to the different cooling rates between the DSC and HT-CLSM measurements and also the temperature difference between the surface of the melt and the bottom of the crucible in the HT-CLSM.

In terms of maximum and average diameter changes of δ ferrite (Figure 4 (c)), the maximum diameter of δ ferrite slowly increases at the beginning, and begins to increase rapidly when the δ ferrite grows to a certain extent. The maximum and average diameter changes of δ ferrite show a similar tendency in the case of slow cooling, while the average diameter of δ ferrite gradually increases during the whole solidification period under a fast cooling rate. As a result, the average diameter of δ ferrite at the end of the solidification stage is approximately 80 μm at the cooling rate of 150 °C/min compared to 460 μm at the cooling rate of 4 °C/min. It can be indicated that the faster cooling rate can result in a larger size of δ ferrite. Moreover, the larger number density of nucleation sites of δ ferrite at the beginning of solidification can be found in the case of a high cooling rate, as shown in Figure 4 (d). The peak of the number density of nucleation sites curves indicates that no new nucleation sites can be formed after that point, and the existing nucleation phases start to grow and merge to form bigger cells. In combination with the evolution of the number density of nucleation sites and the diameter of δ ferrite change during the solidification of steel, we can conclude that a slow cooling rate favored the growth of δ ferrite, whereas a high cooling rate favored the nucleation of δ ferrite.

In conclusion, the size of the grain size will be finer as the cooling rate increases, the morphology comprises smaller grains and the solidification behavior will commerce faster. This information can guide the actual continuous casting process of DSS S33207s.

Preprints (www.preprints.org) | NOT PEER-REVIEWED | Posted: 8 May 2023 doi:10.20944/preprints202305.0501.v1

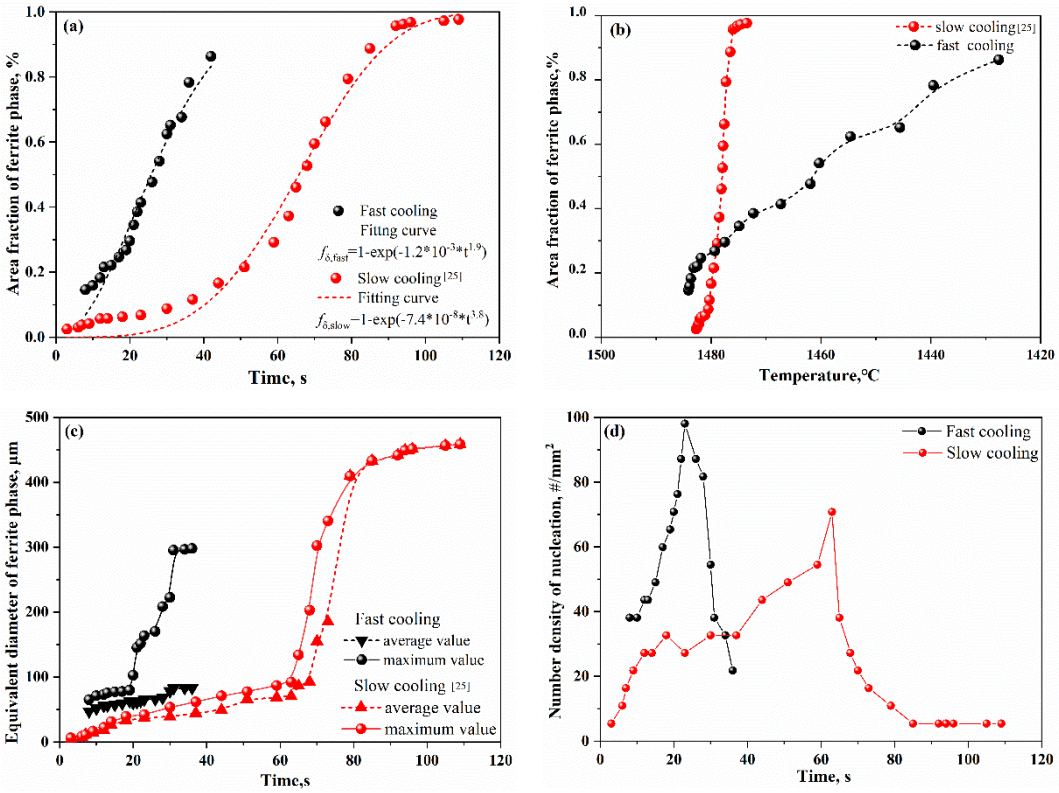

Figure 4. Relationships of area fraction of δ ferrite with time (a) and temperature (b), relationships of average and maximum diameters of δ ferrite with time (c), and relationships of the number density of nucleation sites with time (d). The experimental data of the slow cooling condition in (a) to (c) are taken and adapted from Ref. [25].

3.2. Influences of cooling rates on the microstructures

In this section, the microstructure as well as the chemical composition of the S33207 steel after solidification with different cooling rates is presented briefly in this section.

3.2.1. Steel specimen with a slow cooling rate of 4 ºC/min

Figure 5 presents the typical morphology of the S33207 steel after solidification with a cooling rate of 4 °C/min. It is seen that solidified surface shows a 'bumpy' morphology which presents in Fig.5(a), however, there is no clear segregation of chemical elements, all the element maps presented in Fig.5 (b) to (i) shows an almost homogeneous distribution. In order to see the detailed microstructure and chemical composition evolution, a line scan analysis of the main elements in the steel with the same cooling condition has been presented in Figure 6. In order to see the trend more clearly, the atomic% of each main element is used in this line scan. It is seen that there is a main variation of Fe, Cr and O at each specific location on the solidified surface, and the variation trend of Fe and Cr always correspond with each other at the same location. This fact can lead to a basic understand that the 'bumpy' surface morphology is either due to the chemical element variation or precipitate and inclusion (i.e. oxide and nitride) formation in the bulk under the surface. Detailed consideration can be investigated in the future work.

Preprints (www.preprints.org) | NOT PEER-REVIEWED | Posted: 8 May 2023 doi:10.20944/preprints202305.0501.v1

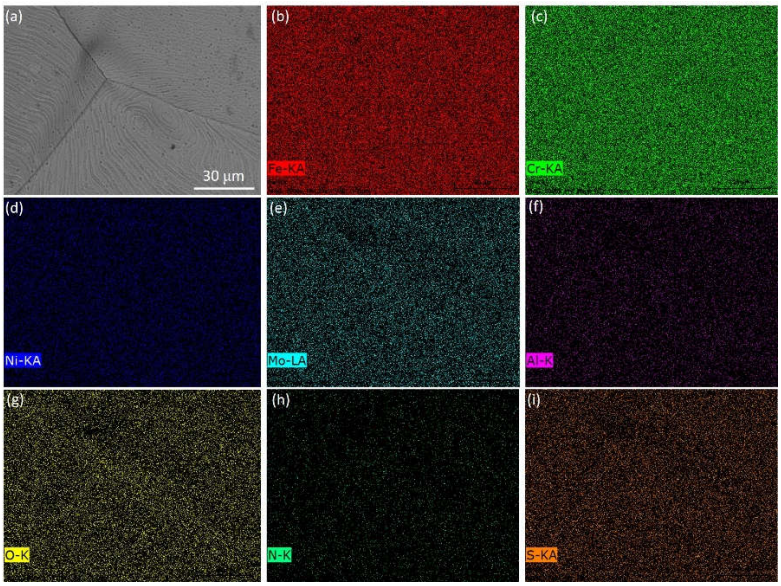

Figure 5. Typical morphology and chemical element maps of S33207 steel after solidification with a cooling rate of 4 ºC/min, (a) SEM images, and (b) to (i) chemical maps of Fe, Cr, Ni, Mo, Mn, Al, O, N, S elements.

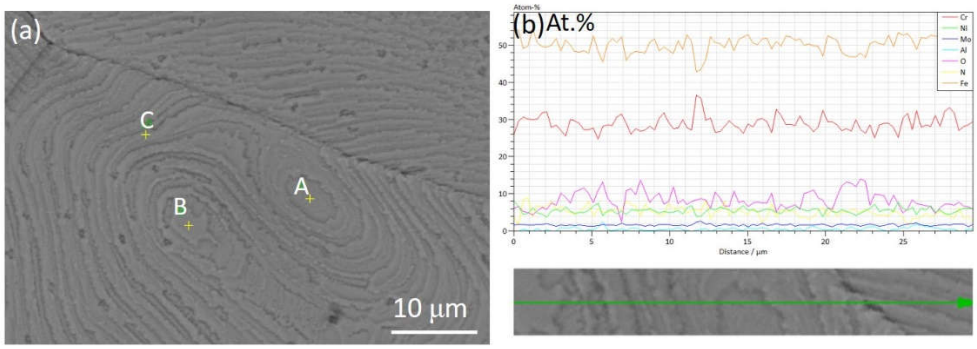

Figure 6. SEM image and line scan of S33207 steel after solidification with a cooling rate of 4 ºC/min, (a) morphology image, and (b) line scan of Fe, Cr, Ni, Mo, Mn, Al, O, and N elements.

In order to see the detailed composition of all elements presented as mass.%, the chemical content of positions A, B, and C in Fig.6(a) is presented in Table 2. It is seen the variation is rather small since there is almost a single bcc phase after the solidification of a slow cooling rate, and the finding is consistent with the above line scan and chemical mapping analysis.

Table 2. Chemical compositions of different locations of S33207 samples with 4 ºC/min cooling rate.

Point in	Chemical elements (mass.%)											
Fig.6(a)	N*	O*	Al	Si	Ti	V	Cr	Mn	Ni	Nb	Mo	Fe
A	1.08	1.40	0.20	0.22	0.01	0.03	29.30	0.58	7.03	0.07	2.94	Bal.
B	0.96	1.65	0.04	0.54	0.01	0.15	30.85	0.46	6.02	0.06	3.08	Bal.
C	1.19	1.93	0.06	0.22	0.01	0.03	29.69	0.52	6.71	0.07	2.96	Bal.

*Qualitative analysis of light elements N and O.

In addition, there are also many tiny particles with concave morphology on the solidified surface with a cooling rate of 4 ºC/min, SEM-EDS line scan analysis result is shown in Figure 7. It is clearly seen that the particles are Al_2O_3. According to the HT-CLSM observation, it is not the non-metallic

Preprints (www.preprints.org) | NOT PEER-REVIEWED | Posted: 8 May 2023 doi:10.20944/preprints202305.0501.v1

inclusion formed in the liquid, the formation could be due to either surface re-oxidation or undertaken of O to the sample surface.

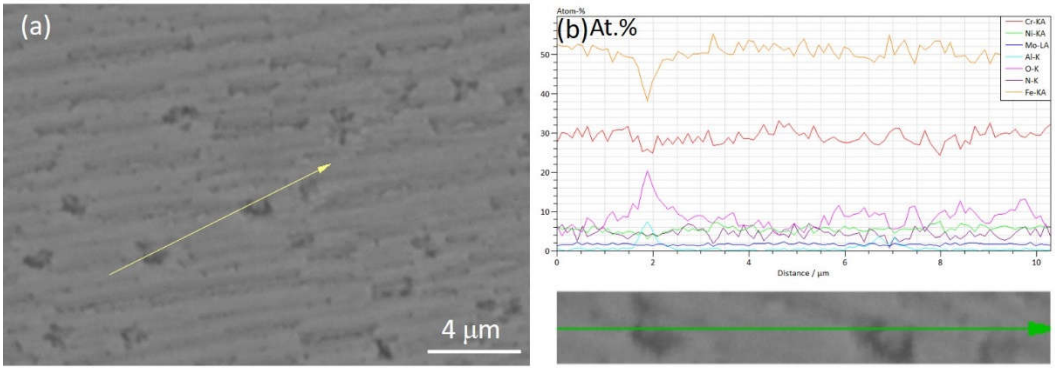

Figure 7. SEM image and line scan of local particles on the S33207 steel surface with a cooling rate of 4 ºC/min, (a) morphology image, and (b) line scan of Fe, Cr, Ni, Mo, Mn, Al, O, and N elements.

3.2.2. Steel specimen with a fast cooling rate of 150 ºC/min

The typical morphology of the steel surface after solidification with 150 ºC/min has been presented in Figure 8. It is clearly seen that the dendrite microstructure can be observed. This microstructure is believed to be formed due to the fast cooling rate, and is not observed in the case with a slow cooling rate of 4 ºC/min. In order to know the chemical composition of each location, SEM-EDS point analysis as well as a line scan has been performed, line scan result can be seen in Figure 9. It is seen that the variation of fcc-stabilize elements (e.g. Ni, N) and bcc-stabilize elements (e.g. Cr) correspond with each other, to distinguish the austenite and ferrite phases. Figure 9 (c) to (j) shows the chemical maps of different elements (i.e. Fe, Cr, Ni, Mo, Mn, N, Nb and V). The concentration of different elements in these maps is not so obvious, which can indicate that the difference of elements at each location is not so large after the solidification. Detailed EDS data of each point is summarized in Table 3, points 2 and 3 hold a relatively higher range of Cr, and a lower range of Ni which can indicate to be the bcc phase. Alternatively, points 1 and 4 hold the higher Ni and lower Cr which can be recognized as fcc-phase. It is worth to be mentioned that in the solidified microstructure, the faction of austenite (fcc) is really not high, which has been confirmed by a separate work using electron backscatter diffraction (EBSD) [25]. This fact is due to the loss of nitrogen during solidification as well as lacking post-heat treatment for austenite growth. Potential solution using a mixed Ar-N_2 gas instead of pure Ar, and adding the isothermal aging process at approximately 1000-1150 ºC will favor the balance of the fraction of austenite and ferrite.

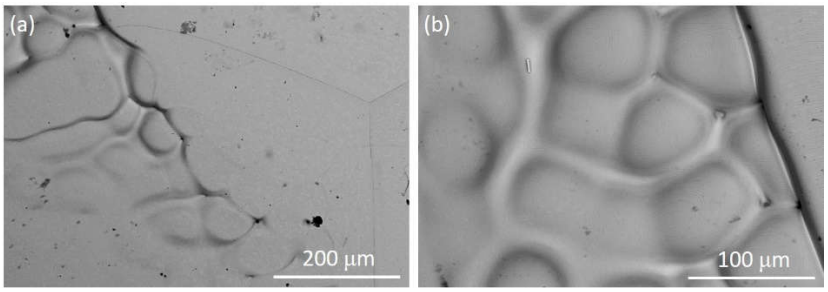

Figure 8. Typical morphology of S33207 after solidification with a cooling rate of 150 ºC/min, (b) is a magnification of a local place in (a).

Preprints (www.preprints.org) | NOT PEER-REVIEWED | Posted: 8 May 2023 doi:10.20944/preprints202305.0501.v1

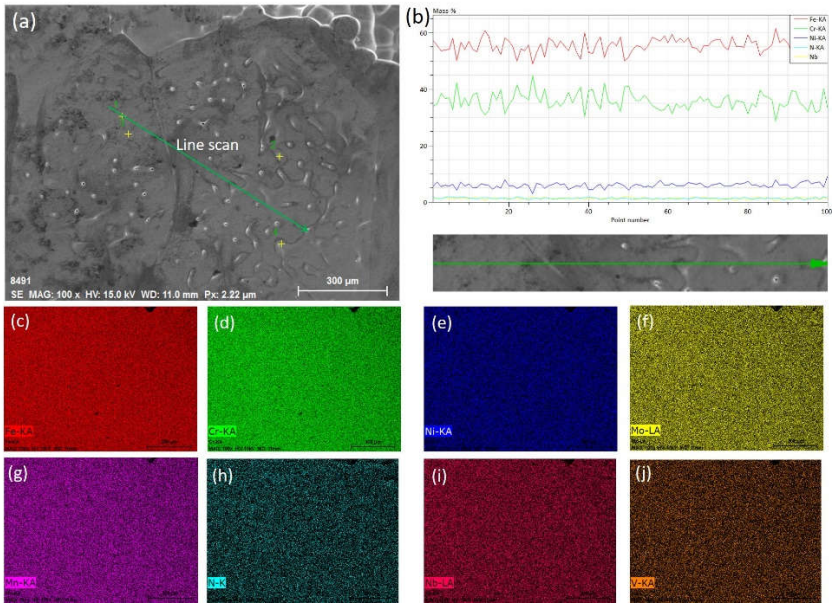

Figure 9. Typical morphology and chemical analysis of S33207 steel after solidification with a cooling rate of 150 ºC/min, (a) SEM images, (b) line scan result, (c) to (j) chemical maps of Fe, Cr, Ni, Mo, Mn, N, Nb and V elements.

Table 3. Chemical compositions of different locations of S33207 samples after solidification.

Point in	Chemical elements (mass.%)										
Fig.5(a)	N*	Al	Si	Ti	V	Cr	Mn	Fe	Ni	Nb	Mo
1	0.38	0.02	0.27	0.02	0.03	32.51	0.34	56.69	6.43	0.10	3.22
2	0.22	0.03	0.13	0.02	0.15	41.83	0.54	47.43	5.59	0.06	3.99
3	0.33	0.07	0.24	0.01	0.02	35.55	0.46	54.23	5.57	0.09	3.41
4	0.34	0.12	0.39	0.01	0.03	30.18	0.37	58.47	6.93	0.16	3.00

*Qualitative analysis of light element N.

4. Conclusions

In this study, the effect of cooling rate on the solidification microstructure of hyper duplex stainless steel S33207 was studied by HT-CLSM. The solidification process of S33207 steel and the formation and growth characteristics of δ ferrite phase were clarified. The main conclusions are as follows: higher cooling rates lead to larger undercooling and increased undercooling leads to finer microstructures of steel. As the cooling rate increased, the solid's microstructure was finer, and the solidification behavior in the body of the liquid pool would commerce more rapidly. As the temperature decreased, the liquid phase first solidified into δ-ferrite and after solidification is complete, the δ-ferrite would remain for a while and then partially transformed into γ. The area fraction of δ ferrite during solidification of S33207 steels at a cooling rate of 4 °C/min can be expressed as $f_{\delta,\text{slow}} = 1 - \exp(-7.4\times10^{-8}\times t^{3.4})$ and at a cooling rate of 150 °C/min can be expressed as $f_{\delta,\text{fast}} = 1 - \exp(-1.2\times10^{-3}\times t^{1.9})$. A slow cooling rate favored the growth of δ ferrite, whereas a high cooling rate favored the nucleation of δ ferrite. These findings could provide guidelines for the solidification control of the advanced hyper duplex stainless steel production.

Author Contributions: Conceptualization, W.M.; data curation, Y.W.; methodology, investigation, preparation for the original draft, Y.W. and W.M.; manuscript review and editing, funding acquisition, project administration and submission, W.M.. All authors have read and agreed to the published version of the manuscript.

Funding: W. Mu would like to acknowledge the Swedish Foundation for International Cooperation in Research and Higher Education (STINT, Project No. PT2017-7330 & IB2022-9228), VINNOVA (No. 2022-01216), SSF Strategic Mobility Grant (SM22-0039) and the Swedish Steel Producers' Association (Jernkontoret), in particular, Axel Ax:-son Johnsons forskningsfond, Prytziska fonden nr 2, and Gerhard von Hofstens Stiftelse för Metallurgisk forskning for the financial support. Y. Wang would like to acknowledge the National Natural Science Foundation of China (No. U21A20113 and 52074198) and Japan Society for the Promotion of Science (JSPS) for the research support in Tohoku University (Japan).

Data Availability Statement: The data presented in this study are available on request from the corresponding author

Acknowledgments: Prof. Hiroyuki Shibata and Assoc. Prof. Sohei Sukenaga from IMRAM, Tohoku University (Japan) are acknowledged for supporting the HT-CLSM measurement.

Conflicts of Interest: The authors declare that they have no known competing financial interest or personal relationship that could have appeared to influence the work reported in this paper.

References

1. H. Qu, H. Hou, P. Li, S. Li, and X. Ren,The effect of thermal cycling in superplastic diffusion bonding of heterogeneous duplex stainless steel, *Materials & Design* **2016**, 96, 499-505.
2. N. Pettersson, S. Wessman, S. Hertzman, and A. Studer,High-temperature phase equilibria of duplex stainless steels assessed with a novel in-situ neutron scattering approach, *Metall. Mater. Trans. A* **2017**, 48, 1562-1571.
3. J. Tucker, M.K. Miller, and G.A. Young,Assessment of thermal embrittlement in duplex stainless steels 2003 and 2205 for nuclear power applications, *Acta Mater.* **2015**, 87, 15-24.
4. T. Karahan, H.E. Emre, M. Tümer, and R. Kacar,Strengthening of AISI 2205 duplex stainless steel by strain ageing, *Materials & Design* **2014**, 55, 250-256.
5. M. Gholami, M. Hoseinpoor, and M.H. Moayed,A statistical study on the effect of annealing temperature on pitting corrosion resistance of 2205 duplex stainless steel, *Corrosion Science* **2015**, 94, 156-164.
6. P. Kangas and G.C. Chai. Use of advanced austenitic and duplex stainless steels for applications in oil & gas and process industry. *Advanced Materials Research*. **2013**. 794, 645-669.
7. G. Chai and P. Kangas,New hyper duplex stainless steels, *Duplex World* **2010**, 1043-1054.
8. K. Göransson, M.L. Nyman, M. Holmquist, and E. Gomes,Sandvik SAF 2707 HD®(UNS S32707): a hyper-duplex stainless steel for severe chloride containing environments, *Metallurgical Research & Technology* **2007**, 104, 411-417.
9. X.Q. Xu, M. Zhao, Y.R. Feng, F.G. Li, and X. Zhang,A Comparative Study of Critical Pitting Temperature (CPT) of Super Duplex Stainless Steel S32707 in NaCl Solution, *Int. J. Electrochem. Sci* **2018**, 13, 4298-4308.
10. J.O. Nilsson,Super duplex stainless steels, *Materials science and technology* **1992**, 8, 685-700.
11. D. Steiner Petrovič, M. Pirnat, G. Klančnik, P. Mrvar, and J. Medved,The effect of cooling rate on the solidification and microstructure evolution in duplex stainless steel: a DSC study, *Journal of thermal analysis and calorimetry* **2012**, 109, 1185-1191.
12. W. Mu, H. Mao, P.G. Jönsson, and K. Nakajima,Effect of carbon content on the potency of the intragranular ferrite formation, *Steel Res. Int.* **2016**, 87, 311-319.
13. H. Shibata, Y. Arai, M. Suzuki, and T. Emi,Kinetics of peritectic reaction and transformation in Fe-C alloys, *Metall. Mater. Trans. B* **2000**, 31, 981-991.
14. Y. Wang, Q. Wang, and W. Mu,In Situ Observation of Solidification and Crystallization of Low-Alloy Steels: A Review, *Metals* **2023**, 13, 517.
15. X. Shi, S.C. Duan, W.S. Yang, H.J. Guo, and J. Guo,Effect of cooling rate on microsegregation during solidification of superalloy INCONEL 718 under slow-cooled conditions, *Metall. Mater. Trans. B* **2018**, 49, 1883-1897.

16. X. Yan, Q. Xu, and B. Liu,Numerical simulation of dendrite growth in nickel-based superalloy and validated by in-situ observation using high temperature confocal laser scanning microscopy, *Journal of Crystal Growth* **2017**, 479, 22-33.
17. Y. Sun, Y. Zhao, X. Li, and S. Jiao,Effects of heating and cooling rates on δ↔ γ phase transformations in duplex stainless steel by in situ observation, *Ironmaking & Steelmaking* **2019**, 46, 277-284.
18. T. Wang,The effects of cooling rate and alloying elements on the solidification behaviour of continuously cast super-austenitic and duplex stainless steels, **2019**.
19. F.X. Huang, X.H. Wang, J.M. Zhang, C.X. Ji, F. Yuan, and Y. Yan,In situ observation of solidification process of AISI 304 austenitic stainless steel, *J. Iron Steel Res. Int.* **2008**, 15, 78-82.
20. C. Wu, S. Li, C. Zhang, and X. Wang,Microstructural evolution in 316LN austenitic stainless steel during solidification process under different cooling rates, *J. Mater. Sci.* **2016**, 51, 2529-2539.
21. X. Li, F. Gao, J. Jiao, G. Cao, Y. Wang, and Z. Liu,Influences of cooling rates on delta ferrite of nuclear power 316H austenitic stainless steel, *Materials Characterization* **2021**, 174, 111029.
22. Y. Zhang, D. Zou, X. Wang, Y. Li, Y. Jiang, W. Zhang, and L. Tong,Influence of cooling rate on δ-ferrite/γ-austenite formation and precipitation behavior of 18Cr–Al–Si ferritic heat-resistant stainless steel, *Journal of Materials Research and Technology* **2022**, 18, 1855-1864.
23. Y. Zhao, Y. Sun, X. Li, and F. Song, In-situ observation of δ↔ γ phase transformations in duplex stainless steel containing different nitrogen contents, *ISIJ Int.* **2017**, 57, 1637-1644.
24. B.H. Shin, J. Park, J. Jeon, S.B. Heo, and W. Chung, Effect of cooling rate after heat treatment on pitting corrosion of super duplex stainless steel UNS S 32750, *Anti-Corrosion Methods and Materials* **2018**, 65, 492-498.
25. Y. Wang, S. Sukenaga, H. Shibata, Q. Wang, and W. Mu, Combination of in-situ confocal microscopy and calorimetry to investigate solidification of super and hyper duplex stainless steels, *Steel Res. Int.* **2023**, in press.
26. W. Mu, H. Shibata, P. Hedström, P.G. Jönsson, and K. Nakajima, Combination of in situ microscopy and calorimetry to study austenite decomposition in inclusion engineered steels, *Steel Res. Int.* **2016**, 87, 10-14.
27. X. Shi, S.C. Duan, W.S. Yang, H.J. Guo, and J. Guo,Effect of cooling rate on microsegregation during solidification of superalloy INCONEL 718 under slow-cooled conditions, *Metall. Mater. Trans. B* **2018**, 49, 1883-1897.
28. G. Liang, C. Wan, J. Wu, G. Zhu, Y. Yu, and Y. Fang,In situ observation of growth behavior and morphology of delta-ferrite as function of solidification rate in an AISI304 stainless steel, *Acta Metallurgica Sinica (English Letters)* **2006**, 19, 441-448.
29. T. Wang, D. Wexler, L. Guo, Y. Wang, and H. Li,In Situ Observation and Phase-Field Simulation Framework of Duplex Stainless-Steel Slab during Solidification, *Materials* **2022**, 15, 5517.
30. J.W. Christian, *The theory of transformations in metals and alloys*. 2002: Newnes.
31. P. Bruna, D. Crespo, R. González-Cinca, and E. Pineda,On the validity of Avrami formalism in primary crystallization, *Journal of applied physics* **2006**, 100, 054907.